

# Reversible voltammetry at cylindrical electrodes: Validity of a one-dimensional model

Haonan Le, Enno Kätelhön, and Richard G. Compton\*

Department of Chemistry, Physical and Theoretical Chemistry Laboratory, Oxford University  
South Parks Road, Oxford, OX1 3QZ, United Kingdom

## Abstract

The cyclic voltammetry of a reversible one-electron-transfer is investigated using finite difference simulations at three electrode geometries: an ‘infinitely long cylinder’ electrode featuring a cylindrical electrode with an infinite length, an ‘annular band’ electrode, whose band-shape electrochemically active area is located around an infinitely long insulating cylinder, and a ‘full cylinder’ electrode which resembles the microwire electrodes widely used in electrochemical experiments with both side and end active. Following the simulation of the infinitely long cylindrical electrode, a polynomial equation is introduced to describe the forward peak potentials at different scan rates. Based on further simulations of the other two electrodes, we find if the lengths of the latter are greater than  $\sim 10^4$  times the radius of the cylinders, the electrochemical reversible cyclic voltammetry of them can be well described by the infinitely long cylinder model with errors of less than 1%.

Keywords: Cylinder electrode; Microwire electrode; Cyclic voltammetry; Finite difference simulation; One dimensional approximation.

---

\*Corresponding author: Richard G. Compton, richard.compton@chem.ox.ac.uk

# 1 Introduction

Microelectrodes are one of the most important tools in electrochemical research<sup>1–6</sup> and are often used to investigate electrochemical reactions and mass transport processes through voltammetry. Among microelectrodes, microcylinder electrodes, often in the forms of microwire electrodes, are frequently used<sup>7–20</sup> partly because of their low cost and ease of fabrication. Cylindrical electrodes show a different voltammetric behaviour from microdisc<sup>21–23</sup> and hemisphere electrodes<sup>24–26</sup> in that they have one micro dimension (the radius) and one macro dimension (the length). This leads to quasi-steady state voltammetry rather than a true steady state under slow voltage scan rate conditions<sup>1;2;27</sup>. The quasi-steady state gives rise to vestigial back peaks in cyclic voltammetry which can have mechanistic value. In addition, the increased electrode area enables microwire electrodes to play an essential role in diverse research areas including environmental sensors<sup>28–30</sup>, medical diagnosis<sup>31–33</sup>, and nano-impact studies<sup>13;34–36</sup>.

Diverse theoretical studies<sup>37–39</sup> have modelled the current responses of infinitely long cylindrical electrodes as illustrated in Figure 1. However, in experimental research utilising microcylinder electrodes, an infinite length of the microcylinder is obviously impossible to realise. The question then arises as to how long either an annular band or a cylinder with an electrochemically active end must be in order that the one dimensional approximation is valid. Therefore, building on our recent work<sup>40</sup> on chronoamperometric current responses of realistic cylinder electrode models identifying finite length effects and the contributions from the disk-like cylinder ‘end’, this work presents studies of simulated cyclic voltammetric currents using the geometries shown in Figure 1. The conditions under which an infinitely long cylindrical electrode model can describe the two other cylinder-like electrodes are clarified.

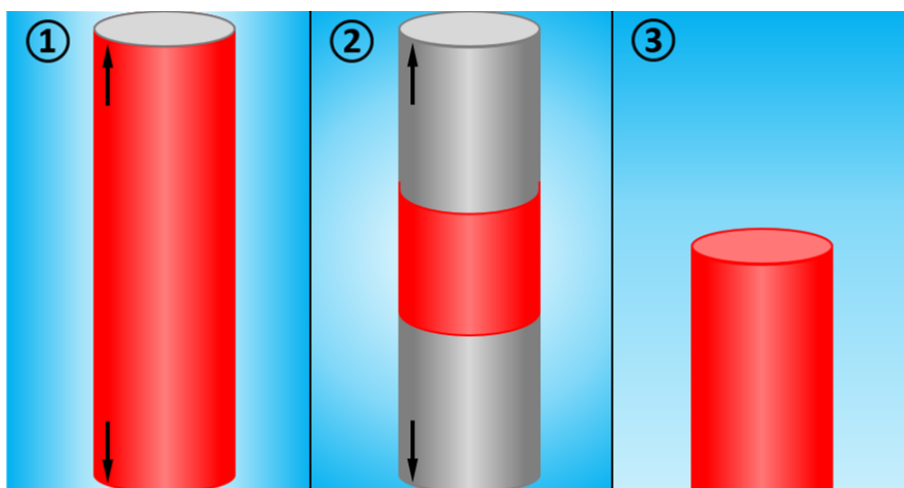


Figure 1: Illustrations of the models investigated: ① the ‘infinitely long cylinder’ electrode model, ② the ‘annular band’ electrode model, ③ the ‘full cylinder’ electrode model. The black arrows in the figures represent infinitely expanding areas.

## 2 Theory and Simulation

In the following section, we introduce the theoretical models, the dimensionless parameters, and the computational methods used in this work. Please refer to recent work<sup>40</sup> for all details beyond the below summary.

### 2.1 Theoretical Models

We investigate the cyclic voltammetry of a single-electron-transfer reaction, as shown in Equation (1), at the three different cylinder-like electrode geometries shown in Figure 1.



The first model, the ‘infinitely long cylinder’ electrode model, is an infinite cylinder with the electrochemically active area at the side of the cylinder. The second model is the ‘annular band’ electrode model, where the electrochemically active area of length  $l$  is at the side of an infinitely long insulating cylinder. Finally, the third model is the ‘full cylinder’ electrode model with the side and the end of the cylinder being electrochemically active.

The initial concentrations  $c_A^*$  of the analyte  $A$  are assumed homogeneous before a potential is applied, and the initial concentration of  $B$  is set to 0 in all simulated space. Assuming a sufficiently high electrolyte concentration, the mass transport is considered exclusively to be diffusion and can be described by the diffusion equation, which is shown in Equation (2) in cylindrical coordinates  $(r, z, \phi)$ :

$$\frac{\partial c}{\partial t} = D\nabla^2 c = D\left(\frac{\partial^2 c}{\partial r^2} + \frac{1}{r}\frac{\partial c}{\partial r} + \frac{\partial^2 c}{\partial z^2} + \frac{1}{r^2}\frac{\partial^2 c}{\partial \phi^2}\right) \quad (2)$$

where  $c$  is the concentration of any species at a certain point,  $t$  is the time,  $D$  is the diffusion coefficient of  $A$ ,  $r$  is the radial distance,  $z$  is the axial distance, and  $\phi$  is the angle around the  $z$ -axis of the plane set by the  $r$ -axis and the  $z$ -axis.

In the ‘infinitely long cylinder’ electrode model, the horizontal symmetry and rotational symmetry for the  $z$ -axis result in the independence of the concentration of the axial distance  $z$  and the angle  $\phi$ . Therefore, this system can be modelled using a one-dimensional coordinate system  $(r)$ , and Equation (2) can be simplified to:

$$\frac{\partial c}{\partial t} = D\left(\frac{\partial^2 c}{\partial r^2} + \frac{1}{r}\frac{\partial c}{\partial r}\right) \quad (3)$$

Similarly, the rotational symmetries around the  $z$ -axes in the ‘annular band’ electrode model and the ‘full cylinder’ electrode model lead to the simplification of Equation (2) can be simplified to:

$$\frac{\partial c}{\partial t} = D \left( \frac{\partial^2 c}{\partial r^2} + \frac{1}{r} \frac{\partial c}{\partial r} + \frac{\partial^2 c}{\partial z^2} \right) \quad (4)$$

In the subsequent simulations, the current responses and the concentration profiles are recorded and analysed for varied lengths of the electrochemically active areas. The electrode process at the electrochemically active area is described by the Nernst equation:

$$E = E_{A/B}^0 + \frac{RT}{F} \ln \left( \frac{c_A^0}{c_B^0} \right) \quad (5)$$

where  $E$  is the electrode potential,  $E_{A/B}^0$  is the formal potential of the  $A/B$  redox reaction,  $R$  is the Universal Gas Constant,  $T$  is the temperature,  $F$  is the Faraday constant, and  $c_A^0$  and  $c_B^0$  are the concentration of  $A$  and  $B$ , respectively, at the electrode surface.

In the cyclic voltammetric simulations,  $E$  are applied to the electrochemically active areas in a constantly varying way shown in Equation (6):

$$E(t) = \begin{cases} \pm \nu t + E(t_0) & \text{when } t \leq t_h \\ \mp \nu(t - t_h) + E(t_h) & \text{when } t > t_h \end{cases} \quad (6)$$

where  $E(t)$  is the potential applied at  $t$  time point,  $E(t_0)$  is the initial potential applied at the beginning of the simulation,  $t_h$  is the time at which the scan is reversed, and  $\nu$  is the scan rate of the potential applied.

### 2.1.1 The ‘Infinitely Long Cylinder’ Electrode Model

As shown in ① in Figure 2, the radius of the infinitely long cylinder is  $r_e$ . The electrochemically active area is shown in red, and the analyte  $A$  is shown in blue.

The boundary conditions for the simulation are shown in ② in Figure 2, where we set the initial concentration of  $A$  to  $c_A^*$  and that of  $B$  to 0:

$$t = 0, \quad r_e \leq r \leq r_{max} : \quad c_A = c_A^*, c_B = 0 \quad (7)$$

For  $t > 0$ , the concentration variation at the electrode surface follows the Nernst equilibrium as previously stated. No-flux boundaries are set at the far end of the simulated space:

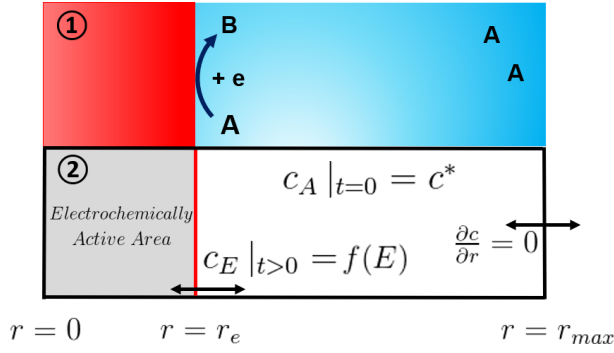


Figure 2: Cross-sectional illustration (①) and boundary conditions (②) of the ‘infinitely long cylinder’ electrode model.  $c$  is the concentration of any species at a certain space,  $c_A$  is the concentration of the analyte  $A$  for all of the points within the simulated space,  $c_A^*$  is the initially homogeneous concentration of the analyte  $A$ ,  $c_E$  is the concentration of the analyte  $A$  for points at the surface of the electrochemically active area,  $r_e$  is the radius of the cylinder, and  $r_{max}$  is the boundary of the simulated space in the  $r$ -axis.

$$t > 0, \quad r = r_{max} : \quad \frac{\partial c}{\partial r} = 0 \quad (8)$$

with the simulated space being a function of the total simulation time  $t_{sim}$ :

$$\begin{cases} r_{max} = r_e + x_{sim} \\ x_{sim} = 6\sqrt{Dt_{sim}} \end{cases} \quad (9)$$

where  $x_{sim}$  is large enough to enable the concentration changes at the electrode surface to be independent on the boundary at the far end<sup>41</sup>.

Following Fick’s first law and Faraday’s law, we can calculate the current responses in the ‘infinitely long cylinder’ electrode model as:

$$I_{ILC} = Fj_{ILC} \quad \text{where} \quad j_{ILC} = -2\pi l_e r_e D \left. \frac{\partial c_A}{\partial r} \right|_{r=r_e} \quad (10)$$

where  $I_{ILC}$  is the current,  $j_{ILC}$  is the flux of the analyte  $A$ , and  $l_e$  is the length of the cylinder if we only extract a fragment of the infinitely long cylinder.

### 2.1.2 The ‘Annular Band’ Electrode Model

As shown in Figure ① in Figure 3, the radius and length of the electrochemically active area in the infinitely long cylinder model is  $r_e$  and  $l_e$ , respectively. The area shown in grey is the insulating area.

The boundary conditions for the simulation are shown in ② in Figure 3. Before applying the potential, the initial concentrations of  $A$  and  $B$  are set to  $c^*$  and 0:

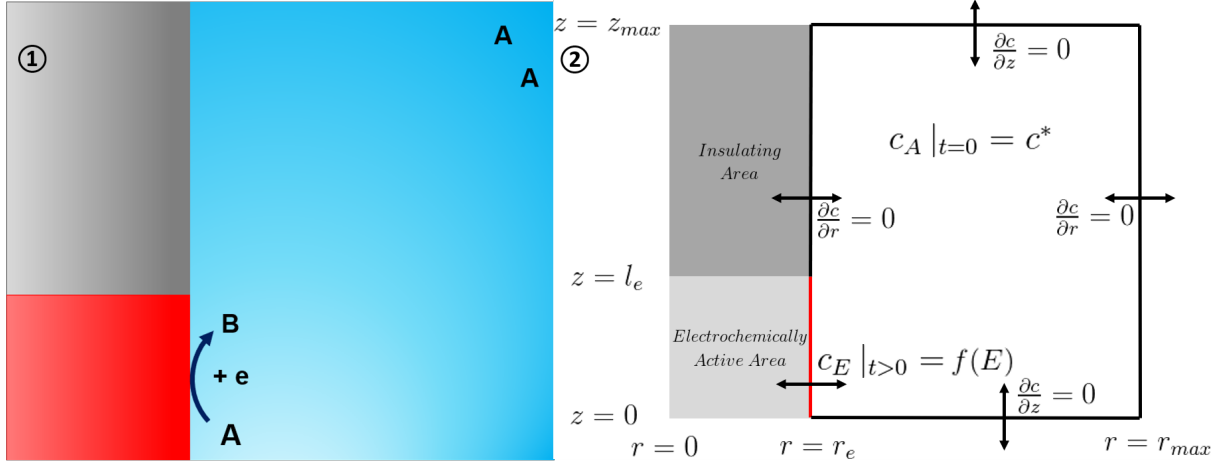


Figure 3: Cross-sectional illustration (①) and boundary conditions (②) of the ‘annular band’ electrode model adapted from a plot in a recent work.  $z_{max}$  is the boundary of the simulated space in the  $z$ -axis,  $l_e$  is the length of the annular band in the  $z$ -axis.

$$t = 0, \quad r_e \leq r \leq r_{max}, \quad 0 \leq z \leq z_{max} : \quad c_A = c_A^*, c_B = 0 \quad (11)$$

For  $t > 0$ , the boundary conditions at the electrochemically active area and everywhere else correspond to the Nernst equilibrium and the no-flux limits, respectively. The no-flux boundaries are:

$$\begin{cases} t > 0, & r = r_e, l_e < z \leq z_{max} : & \frac{\partial c}{\partial r} = 0 \\ t > 0, & r = r_{max}, 0 \leq z \leq z_{max} : & \frac{\partial c}{\partial r} = 0 \\ t > 0, & z = 0, 0 \leq r \leq r_{max} : & \frac{\partial c}{\partial r} = 0 \\ t > 0, & z = z_{max}, 0 \leq r \leq r_{max} : & \frac{\partial c}{\partial r} = 0 \end{cases} \quad (12)$$

where the simulation spaces and their corresponding simulation time  $t_{sim}$  are:

$$\begin{cases} r_{max} = r_e + x_{sim} \\ z_{max} = l_e + x_{sim} \\ x_{sim} = 6\sqrt{Dt_{sim}} \end{cases} \quad (13)$$

Similar to the previous model, we can calculate the current responses of A for the ‘annular band’ electrode model as:

$$I_{AB} = Fj_{AB} \quad \text{where} \quad j_{AB} = -2\pi r_e D \int_0^{l_e} \frac{\partial c_A}{\partial r} \Big|_{r=r_e} dz \quad (14)$$

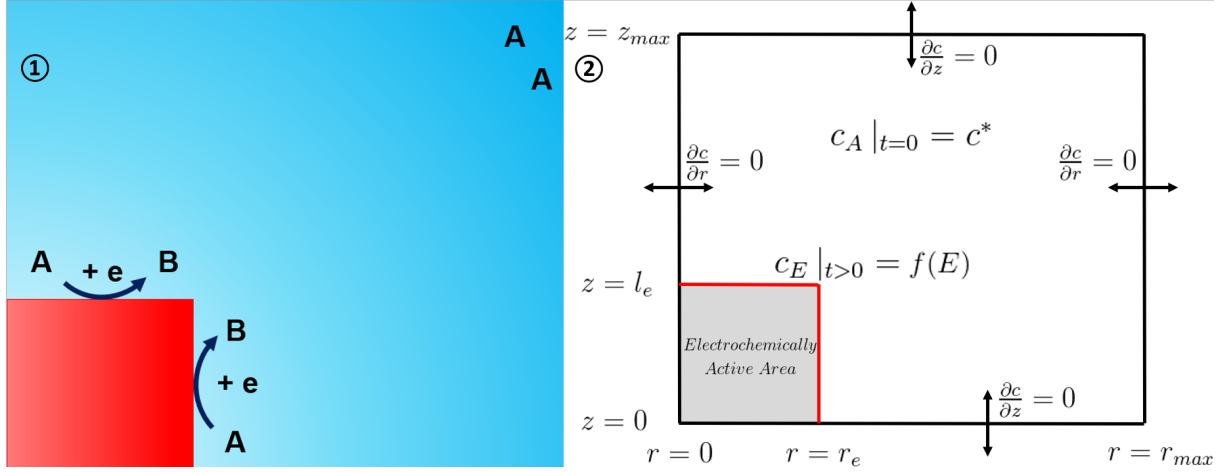


Figure 4: Cross-sectional illustration (①) and boundary conditions (②) of the ‘full cylinder’ electrode model adapted from a plot in a recent work<sup>40</sup>.

where  $I_{AB}$  and  $j_{AB}$  are the current and the flux of the analyte  $A$ , respectively.

### 2.1.3 The ‘Full Cylinder’ Electrode Model

As shown in Figure ① of Figure 4, the side and the end of cylinder in this model are electrochemically active. This model aims to model the microcylinder, or microwire, electrode, which is commonly used in experiments. In this system, diffusion equation is also expressed by Equation 4.

The boundary conditions, shown in Figure ② in Figure 4, demonstrate the modelling details. The concentrations of  $A$  and  $B$  for all of the points in the simulations are initially set as  $c^*$  and 0:

$$t = 0, \quad 0 \leq r < r_e, \quad 0 \leq z < l_e : \quad c_A = c_A^*, c_B = 0 \quad (15)$$

The boundary conditions for the electrochemically active areas follows the Nernst equilibrium. No-flux boundaries are set similarly to Equation 12:

$$\begin{cases} t > 0, & r = r_e, \quad 0 \leq z \leq l_e : & c = 0 \\ t > 0, & z = l_e, \quad 0 \leq r \leq r_e : & c = 0 \end{cases} \quad (16)$$

where the simulation space is:

$$\begin{cases} r_{max} = r_e + x_{sim} \\ z_{max} = l_e + x_{sim} \\ x_{sim} = 6\sqrt{Dt_{sim}} \end{cases} \quad (17)$$

The fluxes and currents of  $A$  towards the side and the end of the cylinder are calculated separately before summed up to the total fluxes  $j_{FC}$  currents  $I_{FC}$  of  $A$ :

$$\begin{cases} I_s = Fj_s & \text{where } j_s = -2\pi r_e D \int_0^{l_e} \frac{\partial c_A}{\partial r} \Big|_{r=r_e} dz \\ I_e = Fj_e & \text{where } j_e = -2\pi D \int_0^{r_e} \frac{\partial c_A}{\partial z} \Big|_{z=l_e} r dr \\ j_{FC} = j_s + j_e \\ I_{FC} = I_s + I_e \end{cases} \quad (18)$$

where  $I_e$  is the current to the end of the cylinder,  $j_e$  is the flux of the analyte  $A$  to the end of the cylinder, and the total current  $I_{FC}$  is the sum of the current towards the side  $I_s$  and the end  $I_e$  of the electrode.

## 2.2 Dimensionless Parameters

Dimensionless parameters are introduced in this section to enable a simple and universal presentation of the simulation results. By adopting dimensionless forms, comparison between different experimental systems can be more straightforward. The transformations are shown in Table 1, where  $\sigma$  and  $\nu$  are the dimensional and dimensionless form of the scan rate of the potential applied.

In dimensionless parameters, the diffusion equation Equation 3 and 4 can be rewritten as:

$$\frac{\partial C_j}{\partial T} = d_j \left( \frac{\partial^2 C_j}{\partial R^2} \right) \quad \text{and} \quad \frac{\partial C_j}{\partial T} = d_j \left( \frac{\partial^2 C_j}{\partial R^2} + \frac{1}{R} \frac{\partial C_j}{\partial R} + \frac{\partial^2 C_j}{\partial Z^2} \right) \quad (19)$$

where  $C_j$  is the dimensionless concentration of the species  $j$ , and  $d_j$  is the dimensionless diffusion coefficient of the species  $j$ , as defined in Table 1.

The current calculations Equation 10, Equation 14, and Equation 18 can be rewritten as:

$$J_{ILC} = -2\pi L_e d_A \frac{\partial C_A}{\partial R} \Big|_{R=1} \quad (20)$$

$$J_{AB} = -2\pi d_A \int_0^{L_e} \frac{\partial C}{\partial R} \Big|_{R=1} dZ \quad (21)$$



Table 1: Transformation of dimensional parameters to dimensionless parameters where  $r_r$  is the reference length of the respective model.

Dimensionless Parameter	Conversion
Concentration of species j	$C_j = \frac{c_j}{c^*}$
Diffusion coefficient of species j	$d_j = \frac{D_j}{D}$
Radial distance	$R = \frac{r}{r_r}$
Axial distance	$Z = \frac{z}{r_r}$
Cylinder length	$L = \frac{l}{r_r}$
Time	$T = \frac{Dt}{r_r^2}$
Potential	$\theta = \frac{F}{RT}(E - E_f^0)$
Current	$J = \frac{I}{F r_r D c^*}$
Scan rate	$\sigma = \frac{r_r^2 F}{D RT} \nu$

$$\begin{cases} J_s = -2\pi d_A \int_0^{L_e} \left. \frac{\partial C}{\partial R} \right|_{R=1} dZ \\ J_e = -2\pi d_A \int_0^1 \left. \frac{\partial C}{\partial Z} \right|_{Z=L_e} R dR \\ J_{FC} = J_s + J_e \end{cases} \quad (22)$$

where  $L_e$  is the dimensionless length of the electrode.

### 2.3 Computational Methods

Codes were developed in *C++* for the simulation models shown in previous sections. The partial differential equations in this work are solved via matrix equations using the finite difference approach. Specifically, the alternating direction implicit (ADI) method<sup>42–44</sup>. Data is processed and visualised via Python scripts using the *NumPy* and *matplotlib* libraries. Please refer to the textbook<sup>41</sup> and a recent work<sup>40</sup> for more details.

We employ various testing and validation methods<sup>45</sup> as reported in the Supplementary Information including convergence studies and studies of error of mass conservation.

## 3 Results and Discussion

In this section, we present and discuss the simulation results for different models. The ‘infinitely long cylinder’ electrode model is addressed first to develop empirical equations for the peak separation ( $\Delta E_{pp}$ ) and the forward peak currents ( $I_p$ ) for a reversible electrochemical reaction. The ‘annular band’ electrode

model and the ‘full cylinder’ electrode model are discussed subsequently to explore the differences and similarities between the cylinder-like models and to further investigate how long a microcylinder should be for its currents to be described accurately by the ‘infinitely long cylinder’ electrode model.

### 3.1 The ‘Infinitely Long Cylinder’ Electrode Model

For this model, simulations were computed for various scan rates  $\sigma$ . At high scan rates,  $\Delta E_{pp}$  and  $I_p$  in the cyclic voltammetric current responses for an infinitely long cylinder can be described by<sup>46</sup>:

$$\begin{cases} \Delta E_{pp} = 2.218 \frac{RT}{F} \\ I_p = -0.446 F A c^* \sqrt{\frac{FD\nu}{RT}} \end{cases} \quad (23)$$

where  $A$  is the surface area of the electrode. At low scan rates, two empirical equations<sup>37</sup> have been reported by Aoki et al to describe the forward peak potentials  $E_{fpp}$  and  $I_p$ :

$$\begin{cases} \log_{10}(p) = \frac{-E_{fpp}^4 - 40}{100} + \frac{2.75}{E_{fpp}^4 - 1.41} \\ I_p = \frac{Fc^*D(0.446p + 0.335p^{0.15})}{r} \\ p = \sqrt{\frac{Fr^2\nu}{RTD}} \end{cases} \quad (24)$$

where the percentage errors of the empirical equation for  $E_{fpp}$  are reported in the same work to be less than 0.17 as a dimensionless value, which is 4mV at 298K, for  $\log_{10}(p) < -2$ . The errors of the empirical equation for  $I_p$  are reported<sup>37</sup> to be less than 2% for any  $p$ .

The simulated dimensionless forward peak position  $\theta_{fpp}$  and forward peak current  $J_p$  are plotted in ① and ② in Figure 5 compared with the equations introduced previously. As shown in ① in Figure 5, the Aoki equation for  $\theta_{fpp}$ <sup>37</sup> can describe the simulated  $\theta_{fpp}$  for  $\log_{10}(p) < -2$ . However, for large scan rates, there is a increased difference between the Aoki equation for  $\theta_{fpp}$  and the simulated  $\theta_{fpp}$  as scan rate increases. To describe the  $\theta_{fpp}$  over a wider range of scan rates, we perform the fitting of polynomial equation to the simulated data. The equations are shown with 5th, 6th and 7th order polynomial fittings:

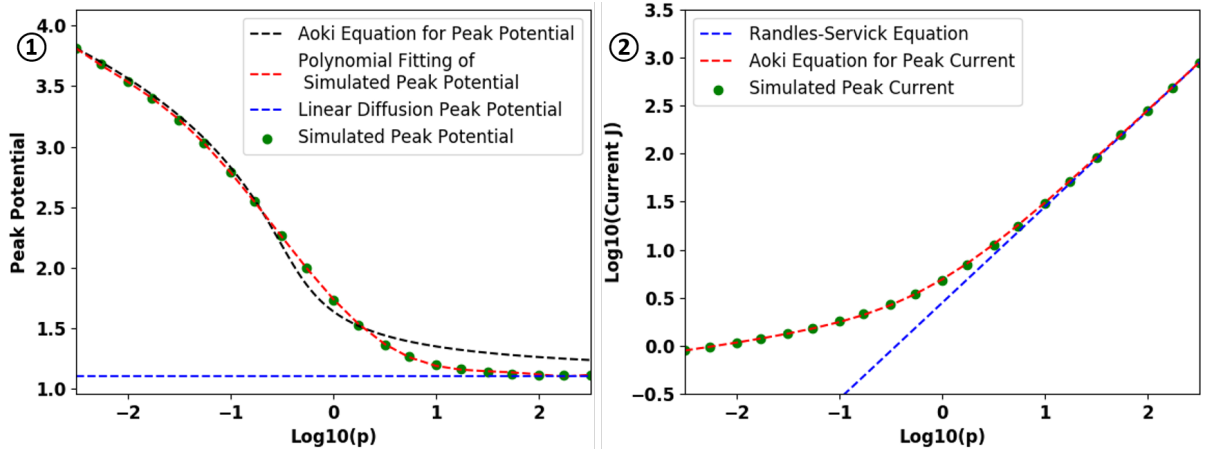


Figure 5: Comparison of the simulated peak potentials (①) and peak currents (②) and the corresponding equations. ① The simulated peak potentials (green dots) are compared with the Aoki equation for the peak potentials (black), the polynomial fitting of the simulated peak potentials (red), and the theoretical peak potential for linear diffusion (blue). ② The simulated peak currents (green) are compared with the Randles-Sevcik equation (blue) and the Aoki equation for the peak current (red).

$$\left\{ \begin{array}{l}
 \begin{array}{l}
 5th \text{ order : } \theta_{fpp} = -0.007374x^5 - 0.01784x^4 + 0.1022x^3 + 0.2187x^2 \\
 \quad \quad \quad - 0.8928x + 1.767 \\
 6th \text{ order : } \theta_{fpp} = 0.003786x^6 - 0.007406x^5 - 0.05259x^4 + 0.1024x^3 \\
 \quad \quad \quad + 0.2964x^2 - 0.8931x + 1.742 \\
 7th \text{ order : } \theta_{fpp} = 0.001118x^7 + 0.003777x^6 - 0.01944x^5 - 0.05252x^4 \\
 \quad \quad \quad + 0.1387x^3 + 0.2963x^2 - 0.9198x + 1.742 \\
 x = \log_{10}(p)
 \end{array}
 \end{array} \right. \quad (25)$$

where the percentage error of the polynomial fitting equation for 5th, 6th and 7th order equations are 3.5%, 1.6%, and 1.2%, respectively.

As shown in ② in Figure 5, the Aoki equation for  $J_p$  can adequately describe the simulated results, and at high scan rates the simulated  $J_p$  and the Aoki equation for  $J_p$  approach the Randles-Sevcik equation.

### 3.2 The ‘Annular Band’ Electrode Model

Simulations were computed for various lengths  $L$  of the electrochemically active area at three different scan rates:  $\sigma = 10^{-5}, 10^0, 10^5$ . As shown in Figure 6, the minimum value of lengths  $L$ , where the differences between the simulated results for forward peak potentials and forward peak currents for this

model and those for the infinitely long cylinder model are less than 1%, are plotted at different scan rates. Figure 6 shows that when the scan rates  $\sigma$  increases, the minimum value of  $L$  for the cyclic voltammograms from this model to resemble those for the infinitely long cylinder model at  $\text{Log}_{10}$  scale decreases almost linearly with the  $\text{Log}_{10}\sigma$ . We infer that this is because the increased  $\sigma$  results in reduce of diffusion layer which gives the additional diffusion field near the insulating areas a smaller impact. Therefore, the minimum value of  $L$  is smaller when the  $\sigma$  increases. It is noticeable that the minimum value of  $L$  for the peak currents are higher than those for peak potentials, which suggested the peak current is a more sensitive indicator comparing to the peak potential in this model.

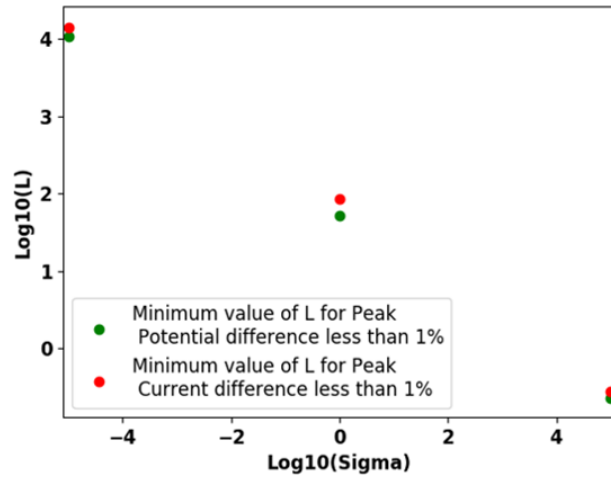


Figure 6: The minimum value of lengths  $L$  where the differences between the simulated results for peak potentials and forward peak currents for the ‘annular band’ model and those for the infinitely long cylinder model are less than 1%.

To present an experimental perspective, a set of typical experimental parameters, shown in Table 2, is used to convert the dimensionless current responses into their dimensional counterparts.

Table 2: Dimensional parameters often used in microelectrode experiments<sup>13;14</sup>

Dimensional parameter	Value
Electrode radius ( $r_e$ )	$3.5\mu m$
Diffusion coefficient ( $D$ )	$10^{-9}m^2/s$
Initial analyte concentration ( $c^*$ )	$1mM$

The minimum value of  $L$  for differences less than 1% are also provided in Table 3. Overall, if the value of  $L$  is greater than  $L = 1.4 \times 10^4$  ( $l = 49mm$  when the radius is  $3.5\mu m$ ), where  $l$  is the dimensional length of the cylinders, for the ‘annular band’ electrode model, the percentage differences between forward peak potential and forward peak current for the ‘annular band’ model and those for the infinitely long cylinder

model are less than 1% for dimensional scan rate in the range from  $2.1 \times 10^{-5}v/s$  to  $2.1 \times 10^5v/s$  for the parameters shown in Table 2.

Table 3: The minimum value of lengths  $L$  and their dimensional counterparts where the differences between the simulated results for peak potentials and forward peak currents for the ‘annular band’ model and those for the infinitely long cylinder model are less than 1%.

$\sigma$	$\nu$ (V/s)	$L$ for $E_{fpp}$	$l$ for $E_{fpp}$ (mm)	$L$ for $I_p$	$l$ for $I_p$ (mm)
$10^{-5}$	$2.1 \times 10^{-5}$	$1.1 \times 10^4$	$3.9 \times 10^1$	$1.4 \times 10^4$	$4.9 \times 10^1$
$10^0$	2.1	$5.3 \times 10^1$	$1.9 \times 10^{-1}$	$8.5 \times 10^1$	$3 \times 10^{-1}$
$10^5$	$2.1 \times 10^5$	$2.3 \times 10^{-1}$	$8.1 \times 10^{-4}$	$2.8 \times 10^{-1}$	$9.8 \times 10^{-4}$

### 3.3 The ‘Full Cylinder’ Electrode Model

Next corresponding simulations were computed for various lengths  $L$  of the electrochemically active area at three different scan rates:  $\sigma = 10^{-5}, 10^0, 10^5$  for the ‘full cylinder’ electrode model. As shown in Figure 7, the minimum value of lengths  $L$ , where the differences between the simulated results for peak potentials and forward peak currents for this model and those for the infinitely long cylinder model are less than 1%, are plotted at different scan rates. Figure 7 shows that when the scan rates  $\sigma$  increases, the minimum value of  $L$  for the cyclic voltammograms of this model resembling those for the infinitely long cylinder model decreases. However, at high  $\sigma$ , the minimum value of  $L$  for the peak currents is much higher than that in the ‘annular band’ model. We assign this difference to the contribution from the top of the cylinder electrode: at high  $\sigma$ , the peak current is much higher than the peak current in the infinitely long cylinder model because the electrochemical reaction at the top of the cylinder contribute to a large amount of the total current responses, which results in larger minimum value of  $L$ .

The minimum value of  $L$  for differences less than 1% are also provided in Table 4. Overall, if the value of  $L$  is greater than  $L = 1.1 \times 10^4$  ( $l = 39mm$  when the radius is  $3.5\mu m$ ) for the ‘full cylinder’ electrode model, the percentage differences between forward peak potential and forward peak current for the ‘full cylinder’ model and those for the infinitely long cylinder model are less than 1% for dimensional scan rate in the range from  $2.1 \times 10^{-5}v/s$  to  $2.1 \times 10^5v/s$  for the parameters shown in Table 2.

## 4 Conclusions

This work has introduced a polynomial empirical equation to describe the cyclic voltammetric currents at infinitely long cylindrical electrodes for reversible electrochemical reactions. By comparing the simulated

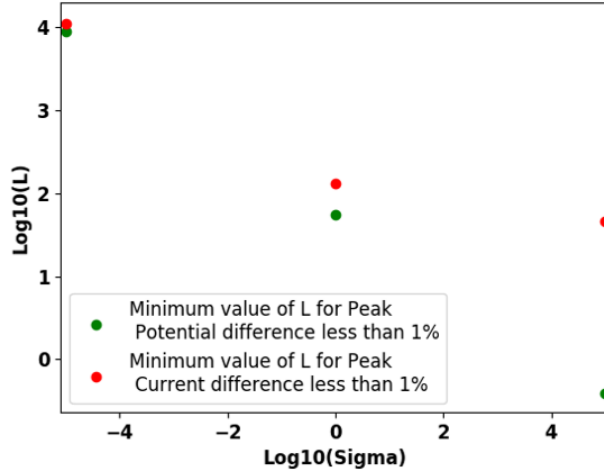


Figure 7: The minimum value of lengths  $L$  where the differences between the simulated results for peak potentials and forward peak currents for the ‘full cylinder’ model and those for the infinitely long cylinder model are less than 1%.

Table 4: The minimum value of lengths  $L$  and their dimensional counterparts where the differences between the simulated results for peak potentials and forward peak currents for the ‘full cylinder’ model and those for the infinitely long cylinder model are less than 1%.

$\sigma$	$\nu$ (V/s)	$L$ for $E_{fpp}$	$l$ for $E_{fpp}$ (mm)	$L$ for $I_p$	$l$ for $I_p$ (mm)
$10^{-5}$	$2.1 \times 10^{-5}$	$9 \times 10^3$	$3.2 \times 10^1$	$1.1 \times 10^4$	$3.9 \times 10^1$
$10^0$	2.1	$5.5 \times 10^1$	$1.9 \times 10^{-1}$	$1.3 \times 10^2$	$4.6 \times 10^{-1}$
$10^5$	$2.1 \times 10^5$	$3.9 \times 10^{-1}$	$1.4 \times 10^{-3}$	4.6	$1.6 \times 10^{-1}$

peak potentials and peak currents for two cylinder-like electrode models with the simulated results for the infinitely long cylinder model, we find that if the length of the cylinder is at least  $1.4 \times 10^4$  times and  $1.1 \times 10^4$  times longer than the radius for the ‘annular band’ electrode model and the ‘full cylinder’ electrode model, respectively, the percentage differences between the simulated cyclic voltammograms for the infinitely long cylinder model and the simulated results for the ‘annular band’ electrode model and the ‘full cylinder’ electrode model are less than 1% for scan rates  $\nu$  in the range from  $2.1 \times 10^{-5} \text{ V/s}$  to  $2.1 \times 10^5 \text{ V} \cdot \text{s}^{-1}$ , that is for instance, if the length of the cylinder is longer than  $49 \text{ mm}$  and  $39 \text{ mm}$ , respectively, when the radius is  $3.5 \mu\text{m}$  and the diffusion coefficient is  $10^{-9} \text{ m}^2 \cdot \text{s}^{-1}$ .

## References

- [1] K. Aoki. Theory of ultramicroelectrodes. *Electroanalysis*, 5(8):627–639, 1993.
- [2] J. Heinze. Ultramicroelectrodes in electrochemistry. *Angewandte Chemie International Edition in*

- English*, 32(9):1268–1288, 1993.
- [3] R. J. Forster. Microelectrodes: new dimensions in electrochemistry. *Chem. Soc. Rev.*, 23:289–297, 1994.
  - [4] R. J. C. Brown and D. J. L. Brett. Microelectrode voltammetry as a high accuracy method for determination of diffusion coefficients. *Microchimica Acta*, 164(3):337–344, 2009.
  - [5] D.E. Tallman. Microelectrodes for voltammetry—a personal historical perspective. *Journal of Solid State Electrochemistry*, 15(7-8):1703–1710, 2011.
  - [6] K. J. Aoki, C. Zhang, J. Chen, and T. Nishiumi. Heterogeneous reaction rate constants by steady-state microelectrode techniques and fast scan voltammetry. *Journal of Electroanalytical Chemistry*, 706:40–47, 2013.
  - [7] P. M. Kovach, W. L. Caudill, D. G. Peters, and R. M. Wightman. Faradaic electrochemistry at microcylinder, band, and tubular band electrodes. *Journal of Electroanalytical Chemistry*, 185(2):285–295, 1985.
  - [8] K. Aoki and H. Kaneko. Theory of irreversible cyclic voltammograms at microcylinder electrodes. *Journal of Electroanalytical Chemistry*, 247(1-2):17–27, 1988.
  - [9] S.T. Singleton, J.J. O’Dea, and J. Osteryoung. Analytical utility of cylindrical microelectrodes. *Analytical Chemistry*, 61(11):1211–1215, 1989.
  - [10] R. Ferrigno, P.F. Brevet, and H.H. Girault. Finite element simulation of the chronoamperometric response of recessed and protruding microdisc electrodes. *Electrochimica Acta*, 42(12):1895 – 1903, 1997.
  - [11] D. Britz, O. Østerby, and J. Strutwolf. Reference values of the chronoamperometric response at cylindrical and capped cylindrical electrodes. *Electrochimica Acta*, 55(20):5629–5635, 2010.
  - [12] S. J. Percival and B. Zhang. Electrocatalytic reduction of oxygen at single platinum nanowires. *The Journal of Physical Chemistry C*, 117(27):13928–13935, 2013.
  - [13] J. Ellison, C. Batchelor-McAuley, K. Tschulik, and R. G. Compton. The use of cylindrical micro-wire electrodes for nano-impact experiments; facilitating the sub-picomolar detection of single nanoparticles. *Sensors and Actuators B: Chemical*, 200:47 – 52, 2014.

- [14] C. Batchelor-McAuley, J. Ellison, K. Tschulik, P. L. Hurst, R. Boldt, and R. G. Compton. In situ nanoparticle sizing with zeptomole sensitivity. *Analyst*, 140:5048–5054, 2015.
- [15] A. Molina, J. González, E. Laborda, and R.G. Compton. Analytical solutions for fast and straightforward study of the effect of the electrode geometry in transient and steady state voltammetries: Single- and multi-electron transfers, coupled chemical reactions and electrode kinetics. *Journal of Electroanalytical Chemistry*, 756:1 – 21, 2015.
- [16] S. Eloul, E. Kätelhön, C. Batchelor-McAuley, K. Tschulik, and R. G. Compton. Diffusional impacts of nanoparticles on microdisc and microwire electrodes: The limit of detection and first passage statistics. *Journal of Electroanalytical Chemistry*, 755:136 – 142, 2015.
- [17] K. Ngamchuea, C. Lin, C. Batchelor-McAuley, and R. G. Compton. Supported microwires for electroanalysis: Sensitive amperometric detection of reduced glutathione. *Analytical Chemistry*, 89(6):3780–3786, 2017.
- [18] L. Chen, C. Lin, and R. G. Compton. Single entity electrocatalysis: oxygen reduction mediated via methyl viologen doped nafion nanoparticles. *Phys. Chem. Chem. Phys.*, 20:15795–15806, 2018.
- [19] C. Zhang, N. Driver, Q. Tian, W. Jiang, and H. Liu. Electrochemical deposition of conductive polymers onto magnesium microwires for neural electrode applications. *Journal of Biomedical Materials Research - Part A*, 106(7):1887–1895, 2018.
- [20] D. Li, C. Batchelor-McAuley, L. Chen, and R. G. Compton. Voltammetric demonstration of thermally induced natural convection in aqueous solution. *Phys. Chem. Chem. Phys.*, 21:9969–9974, 2019.
- [21] S. Eloul and R. G. Compton. Shielding of a microdisc electrode surrounded by an adsorbing surface. *ChemElectroChem*, 1(5):917–924, 2014.
- [22] J. Ellison, S. Eloul, C. Batchelor-McAuley, K. Tschulik, C. Salter, and R. G. Compton. The effect of insulator nano-sheath thickness on the steady state current at a micro-disc electrode. *Journal of Electroanalytical Chemistry*, 745:66 – 71, 2015.
- [23] K. Cinková, M. Clark, S. V. Sokolov, C. Batchelor-McAuley, Ľ. Švorc, and R. G. Compton. Improving limits of detection. microdisc versus microcylinder electrodes. *Electroanalysis*, 29(4):1006–1013, 2017.



- [24] K. B. Oldham and C. G. Zoski. Comparison of voltammetric steady states at hemispherical and disc microelectrodes. *Journal of Electroanalytical Chemistry and Interfacial Electrochemistry*, 256(1):11–19, 1988.
- [25] C. Amatore and B. Fosset. Equivalence between microelectrodes of different shapes: Between myth and reality. *Analytical Chemistry*, 68(24):4377–4388, 1996.
- [26] Z. Deng, R. Elattar, F. Maroun, and C. Renault. In situ measurement of the size distribution and concentration of insulating particles by electrochemical collision on hemispherical ultramicroelectrodes. *Analytical Chemistry*, 90(21):12923–12929, 2018.
- [27] A. J. Bard, L. R. Faulkner, C. G. Zoski, and J. Leddy. *Electrochemical methods : fundamentals and applications*. New York ; Chichester, second edition. edition, 2001.
- [28] G. Billon and C. M. G. van den Berg. Gold and silver micro-wire electrodes for trace analysis of metals. *Electroanalysis*, 16(19):1583–1591, 2004.
- [29] P. Salaün and C. M. G. van den Berg. Voltammetric detection of mercury and copper in seawater using a gold microwire electrode. *Analytical Chemistry*, 78(14):5052–5060, 2006. PMID: 16841929.
- [30] B. J. Privett, J. H. Shin, and M. H. Schoenfish. Electrochemical sensors. *Analytical Chemistry*, 82(12):4723–4741, 2010.
- [31] K. E. Toghill and R. G. Compton. Electrochemical non-enzymatic glucose sensors:a perspective and an evaluation. 2010.
- [32] J. C. Harfield, C. Batchelor-McAuley, and R. G. Compton. Electrochemical determination of glutathione: a review. *Analyst*, 137:2285–2296, 2012.
- [33] J. R. Windmiller and J. Wang. Wearable electrochemical sensors and biosensors: A review. *Electroanalysis*, 25(1):29–46, 2013.
- [34] M. Pumera. Impact electrochemistry: Measuring individual nanoparticles. *ACS Nano*, 8(8):7555–7558, 2014.
- [35] R. A. S. Couto, L. Chen, S. Kuss, and R. G. Compton. Detection of escherichia coli bacteria by impact electrochemistry. *Analyst*, 143:4840–4843, 2018.
- [36] X. Li, C. Batchelor-McAuley, and R. G. Compton. Silver nanoparticle detection in real-world environments via particle impact electrochemistry. *ACS Sensors*, 4(2):464–470, 2019.

- [37] K. Aoki, K. Honda, K. Tokuda, and H. Matsuda. Voltammetry at microcylinder electrodes: Part i. linear sweep voltammetry. *Journal of Electroanalytical Chemistry and Interfacial Electrochemistry*, 182(2):267 – 279, 1985.
- [38] K. Aoki, K. Honda, K. Tokuda, and H. Matsuda. Voltammetry at Microcylinder Electrodes. 2. Chronoamperometry. *Journal of Electroanalytical Chemistry*, 186(1-2):79–86, 1985.
- [39] A. Szabo, D. K. Cope, D. E. Tallman, P. M. Kovach, and R. M. Wightman. Chronoamperometric current at hemicylinder and band microelectrodes: Theory and experiment. *Journal of Electroanalytical Chemistry*, 217(2):417–423, 1987.
- [40] H. Le, E. Kätelhön, and R. G. Compton. Characterising the nature of diffusion via a new indicator: Microcylinder and microring electrodes. *Journal of Electroanalytical Chemistry*, 855:113602, 2019.
- [41] R. G. Compton, E. Laborda, and K. R. Ward. *Understanding Voltammetry: Simulation of Electrode Processes*. Imperial College Press, 2013.
- [42] D. Peaceman and H. Rachford, Jr. The numerical solution of parabolic and elliptic differential equations. *Journal of the Society for Industrial and Applied Mathematics*, 3:28–41, 1955.
- [43] J. Heinze. Diffusion processes at finite (micro) disk electrodes solved by digital simulation. *Journal of Electroanalytical Chemistry and Interfacial Electrochemistry*, 124:73 – 86, 1981.
- [44] J. A. Alden and R. G. Compton. A general method for electrochemical simulations. 1. formulation of the strategy for two-dimensional simulations. *The Journal of Physical Chemistry B*, 101:8941–8954, 1997.
- [45] E. Kätelhön and R. G. Compton. Testing and validating electroanalytical simulations. *Analyst*, 140:2592–2598, 2015.
- [46] R. G. Compton and C. E. Banks. *Understanding Voltammetry*. World Scientific Press, third edition, 2018.